



Analytical model of a Hall thruster

Trevor Lafleur, Pascal Chabert

► To cite this version:

Trevor Lafleur, Pascal Chabert. Analytical model of a Hall thruster. Physics of Plasmas, 2024, 31 (9), pp.093507. 10.1063/5.0220130 . hal-04705087

HAL Id: hal-04705087

<https://hal.science/hal-04705087v1>

Submitted on 24 Sep 2024

HAL is a multi-disciplinary open access archive for the deposit and dissemination of scientific research documents, whether they are published or not. The documents may come from teaching and research institutions in France or abroad, or from public or private research centers.

L'archive ouverte pluridisciplinaire **HAL**, est destinée au dépôt et à la diffusion de documents scientifiques de niveau recherche, publiés ou non, émanant des établissements d'enseignement et de recherche français ou étrangers, des laboratoires publics ou privés.

Public Domain

Analytical Model of a Hall thruster

Trevor Lafleur*

School of Engineering and Technology, University of New South Wales Canberra, Canberra, ACT 2600, Australia

Pascal Chabert

LPP, CNRS, Ecole Polytechnique, Sorbonne Université, Ecole Polytechnique, F-91128 Palaiseau, France

(Dated: August 28, 2024)

Hall thrusters are one of the most successful and prevalent electric propulsion systems for spacecraft in use today. However, they are also complex devices and their unique $\mathbf{E} \times \mathbf{B}$ configuration makes modelling of the underlying plasma discharge challenging. In this work, a steady-state model of a Hall thruster is developed and a complete analytical solution presented that is shown to be in reasonable agreement with experimental measurements. A characterization of the discharge shows that the peak plasma density and ionization rate nearly coincide and both occur upstream of the peak electric field. The peak locations also shift as the thruster operating conditions are varied. Three key similarity parameters emerge that govern the plasma discharge and which are connected via a thruster current-voltage relation: a normalized discharge current, a normalized discharge voltage, and an amalgamated parameter, $\bar{\alpha}$, that contains all system geometric and magnetic field information. For a given normalized discharge voltage, the similarity parameter $\bar{\alpha}$ must lie within a certain range to enable high thruster performance. When applied to a krypton thruster, the model shows that both the propellant mass flow rate and magnetic field strength must be simultaneously adjusted to achieve similar efficiency to a xenon thruster (for the same thruster geometry, discharge voltage, and power level).

I. INTRODUCTION

Crossed-field plasmas consist of a unique configuration in which a magnetic field is applied perpendicular to an electric field driving the discharge current [1]. Such plasmas are often referred to as $\mathbf{E} \times \mathbf{B}$ discharges and are used in a wide range of applications including Hall thrusters for space propulsion [2, 3], magnetrons for materials processing and advanced manufacturing [4–7], Penning discharges or traps for the storage of charged particles [8–11], and even particle mass separators [12–14]. In many $\mathbf{E} \times \mathbf{B}$ discharges, ions are typically unmagnetized, or only weakly magnetized, while electrons are strongly magnetized. The magnetic field variation across the discharge leads to a strong change in electron mobility that significantly affects the electric field in the plasma. This in turn influences electron transport and energy gain, and consequently overall discharge operation and behaviour. Even without the presence of various microscopic and macroscopic instabilities that are commonly encountered [1, 15], self-consistent discharge modelling can be challenging.

An important type of $\mathbf{E} \times \mathbf{B}$ discharge is a Hall thruster which has emerged as one of the most dominant electric propulsion systems and is used, for example, onboard all Starlink satellites [16, 17]. With the space industry currently experiencing rapid growth, electric propulsion, and Hall thrusters in particular, are expected to become a critical future technology: both for a diverse range of small and large commercial satellite missions, and even for space exploration. Indeed, NASA's proposed lunar

space station, known as the Lunar Orbital Platform-Gateway, will include Hall thrusters for propulsion [18]. A number of key research challenges remain however. For example, there is a growing need to extend the operating envelope to both lower and higher powers, while also exploring the use of alternative propellants [19].

Hall thrusters typically consist of an annular ceramic channel that is open at one end and terminated at the other end by an anode through which propellant gas (historically xenon) is injected [2, 3]. A cathode located externally to the channel emits electrons that are attracted to the anode and which collide with propellant gas to produce a plasma. Positive ions from this plasma are then accelerated by the electric field between the anode and cathode to generate thrust. A radial magnetic field is applied along the length of the channel using permanent magnets/solenoids and a ferromagnetic circuit. This magnetic field helps to both transmit the thrust force to the thruster and impede the motion of electrons across the magnetic field to improve system efficiency.

Ionization within Hall thrusters can be intense and state-of-the-art systems are able to obtain propellant mass utilization efficiencies (ratio of ion beam to input mass flow rates) above 90% [2]. This leads to significant neutral gas depletion in the channel that reduces the electron-neutral collision frequency and which strongly affects electron transport across the magnetic field. This then influences all other plasma properties, such as the ionization rate, as well as the electric field which provides the energy source for maintaining the discharge. This coupling between different discharge properties makes Hall thrusters complex devices where gas ionization and ion acceleration cannot be easily separated into distinct regions as in gridded ion thrusters [2, 20].

* t.lafleur@unsw.edu.au

Together with the sharp change in spatial plasma profiles along the channel, this makes simple models such as volume-averaged approaches unsuitable. Consequently, modelling of Hall thrusters largely focuses on one-, two-, or even three-dimensional simulations [21–28]. Here, various models have been developed by different research groups to study general operation [29, 30], microscopic and macroscopic instabilities [22, 31–34], the importance of shear stresses [35], and plasma-surface interactions [36–38].

While high-fidelity simulations can provide detailed information concerning the underlying physics and operation of Hall thrusters, their complexity naturally makes them numerical experiments. Thus, physical understanding and the clear identification of relevant scaling laws or similarity parameters can be challenging. In this context, similarity parameters are dimensionless quantities constructed by grouping various relevant thruster geometric and/or operating parameters together. Such similarity parameters are analogous to similarity parameters used in fluid dynamics (such as the Mach or Reynolds numbers), and thrusters with identical similarity parameters nominally give self-similar behaviour and performance. Several previous works have made use of simplified models and theoretical arguments, together with historical data, to develop empirical scaling laws to aid in the design of new thrusters [39–41]. Example similarity parameters used include the Melikov-Morozov criterion, which relates the thruster channel length to the ionization mean free path [41], and the ratio of the maximum electron cyclotron frequency to the electron-neutral collision frequency [39]. Starting from a set of kinetic equations, Ref. [41] also identified two amalgamated similarity parameters that together include all major thruster geometric information and operating conditions. Simulation *verification* and *validation* have also become important issues within the plasma physics and electric propulsion communities in recent years [42–44]. Here, validation is an activity that aims to test the validity of the underlying mathematical model and which usually requires a comparison with experimental data. By contrast, verification aims to establish the correctness and accuracy of the mathematical model itself, and which usually entails comparison with a known theoretical solution. Therefore, access to an analytical model of a Hall thruster can help both to uncover important scaling laws and similarity parameters, and serve as a useful verification solution for numerical simulations.

While many detailed Hall thruster models of varying dimensionality already exist within the literature, these models must be solved numerically using sophisticated fluid- or particle-based simulation methods [22–24, 30, 32]. A primary aim of the present paper is to instead establish a pedagogical one-dimensional model that is sufficiently tractable and more transparent to physical understanding. This is achieved through a careful choice of model assumptions that enables a complete analytical solution of the underlying equations. For example,

in contrast with several previous one-dimensional models [21, 33, 37, 45], here only steady-state operation is considered and plasma-wall interactions are neglected. Our work is then somewhat similar to that in Refs. [27, 46] except that a closed form solution is obtained without requiring numerical integration of the model differential equations. This analytical solution then allows several important similarity parameters to be naturally uncovered and which simply and clearly connect thruster performance with major design and operating variables. These similarity parameters include a normalized discharge voltage (ratio of the discharge voltage to a characteristic collisional plasma energy loss), a normalized discharge current (ratio of the discharge current to the equivalent current if all propellant flow was ionized), and a grouped parameter that includes all thruster geometric and magnetic field information. In contrast to previous scaling studies [39, 41], this latter similarity parameter also includes information on the spatial profile of the magnetic field. We begin with a description of the model and its solution in Sec. II, before applying the model to an example Hall thruster in Secs. III and IV where important design and optimization considerations are highlighted. We then end with a careful discussion of the model and results in Sec. V.

II. ANALYTICAL MODEL

A. Model description

While Hall thrusters can exhibit different instabilities (such as the breathing mode [33, 45, 47]) which implies an inherent time dependence, here only a steady-state model representative of time-averaged operation is considered. For some thrusters and operating conditions, large-amplitude instabilities might be sufficiently damped or eliminated [33, 48] which makes this a reasonable assumption. Figure 1 illustrates a Hall thruster where neutral gas is injected into an annular channel from an upstream anode, while electrons are emitted from an external cathode located near the thruster exit plane. A radial (r direction) magnetic field with a given axial (z direction) profile is applied along the length of the channel to impede electron transport towards the anode. Ignoring plasma-wall losses, the one-dimensional continuity equations for neutrals, ions, and electrons are

$$\frac{d}{dz}(n_g v_g) = -n_e n_g K_{iz} \quad (1)$$

$$\frac{d}{dz}(n_i v_i) = \frac{d\Gamma}{dz} = n_e n_g K_{iz} \quad (2)$$

$$\frac{d}{dz}(n_e v_{e,z}) = n_e n_g K_{iz} \quad (3)$$

where n and v are the number density and velocity respectively, $\Gamma = n_i v_i$ is the ion flux, K_{iz} is the ionization rate coefficient, $v_{e,z}$ is the axial electron velocity, $v_g \sim \sqrt{k_B T_g / M}$ is the neutral velocity (assumed constant) with k_B Boltzmann's constant, T_g the neutral gas temperature, and M the neutral mass, and the subscripts g , i , and e refer to neutrals, ions, and electrons. Assuming singly-charged ions and quasi-neutrality, $n_e = n_i = n$ where we have introduced the new variable n to denote the plasma density. The axial ion momentum conservation equation is

$$\frac{d}{dz} (M n v_i^2) = e n E \quad (4)$$

with e the elementary charge and E the axial electric field. Ignoring electron inertia and pressure, and assuming classical electron cross-field transport (see Sec. V), the axial and azimuthal (θ direction) electron momentum conservation equations are

$$0 = -e n E - e n v_{e,\theta} B \quad (5)$$

$$0 = e n v_{e,z} B - m_e \nu_m n v_{e,\theta} \quad (6)$$

Here $v_{e,\theta}$ is the azimuthal electron velocity, B is the radial magnetic field, m_e is the electron mass, and $\nu_m = n_g K_m$ is the electron-neutral momentum transfer collision frequency with K_m the momentum transfer rate coefficient. Ignoring energy transport and wall losses (see Sec. V), the electron energy conservation equation is

$$0 = -e n v_{e,z} E - n n_g K_{iz} \varepsilon_c \quad (7)$$

where $\varepsilon_c = \varepsilon_{iz} + K_{exc} \varepsilon_{exc} / K_{iz} + 3 m_e K_m T_e / (M K_{iz})$ is the average collisional energy loss per electron-ion pair produced [49] with ε_{iz} and ε_{exc} the threshold energies for ionization and excitation respectively, K_{exc} is an average excitation rate coefficient, and T_e is the electron temperature (in units of eV).

B. Model solution

Combining Eqns. 1-2 and integrating allows us to determine the neutral density

$$n_g = \frac{\Gamma_m - \Gamma}{v_g} \quad (8)$$

where $\Gamma_m = Q_m / (M A_{ch})$ with Q_m the input propellant mass flow rate, $A_{ch} = \pi (R_2^2 - R_1^2)$ the cross-sectional area of the annular channel, and R_1 and R_2 the inner and outer radii of the channel respectively. The axial electron velocity is found by combining Eqns. 5 and 6 to obtain

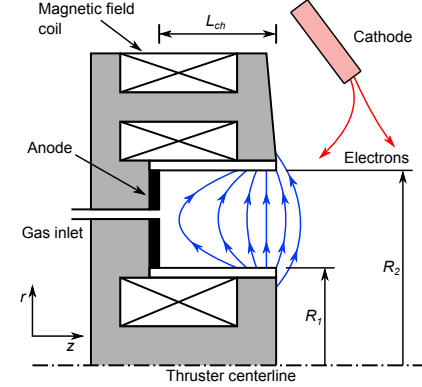


FIG. 1. Side view schematic of a typical Hall thruster.

$$v_{e,z} = - \left(\frac{e n_g K_m}{m_e \omega_{ce}^2} \right) E = -\mu E \quad (9)$$

Here $\mu = e n_g K_m / (m_e \omega_{ce}^2)$ is the electron mobility and $\omega_{ce} = e B / m_e$ is the electron cyclotron frequency. Note that since the magnetic field varies along the channel, the cyclotron frequency is a function of axial position: i.e. $\omega_{ce} = \omega_{ce}(z)$. By combining Eqns. 2-3 and integrating, a discharge current balance equation is obtained from which the electric field can be determined using Eqn. 9

$$E = \frac{\Gamma_d - \Gamma}{n \mu} \quad (10)$$

where $\Gamma_d = I_d / (e A_{ch})$ with I_d the discharge current. Solving for the ionization rate (i.e. $S_{iz} = n n_g K_{iz}$) in Eqn. 7 and substituting the result into Eqn. 2, and then substituting the expressions above for n_g , μ , and E in Eqns. 2 and 4, we find

$$\frac{d\Gamma}{dz} = \left(\frac{m_e v_g \omega_{ce}^2}{e \varepsilon_c K_m} \right) \frac{G (\Gamma_d - \Gamma)^2}{\Gamma^2 (\Gamma_m - \Gamma)} \quad (11)$$

$$\frac{dG}{dz} = \left(\frac{m_e v_g \omega_{ce}^2}{M K_m} \right) \frac{\Gamma_d - \Gamma}{\Gamma_m - \Gamma} \quad (12)$$

Here $G = n v_i^2$ and we have used the fact that $n = \Gamma^2 / G$. Dividing Eqn. 12 by 11 then gives

$$G dG = v^{*2} \frac{\Gamma^2 d\Gamma}{\Gamma_d - \Gamma} \quad (13)$$

where $v^* = \sqrt{e \varepsilon_c / M}$. In general, the average collisional energy loss, ε_c , is a function of the electron temperature, and is shown in Fig. 2 (a) for both xenon and

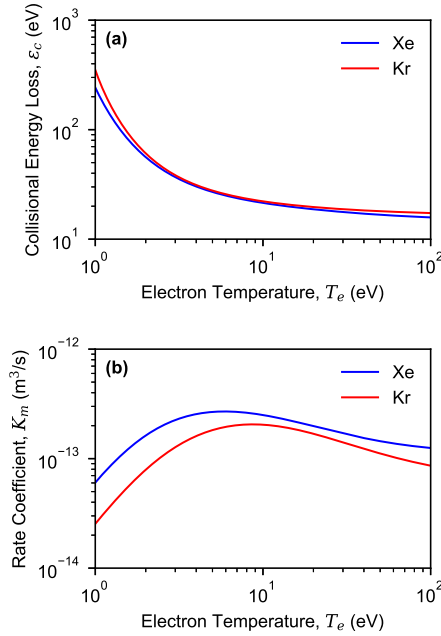


FIG. 2. (a) Average collisional energy loss and (b) electron-neutral momentum transfer rate coefficient as a function of electron temperature for xenon and krypton.

krypton (calculated using cross-section data taken from Ref. [50] and assuming electrons follow a Maxwellian distribution). For electron temperatures above about 5-10 eV, it is seen that the collisional energy loss is relatively constant between 15-25 eV. We therefore make the reasonable assumption that ε_c is fixed and uniform along the channel.

Introducing the normalizations $\chi = \Gamma/\Gamma_d$, $\Omega = G/(v^*\Gamma_d)$, and $\xi = z/L_{ch}$ with L_{ch} the channel length, we integrate Eqn. 13 to obtain

$$\Omega = \sqrt{\Omega_0^2 + \left[\chi_0(2 + \chi_0) - \chi(2 + \chi) - 2 \ln \left(\frac{1 - \chi}{1 - \chi_0} \right) \right]} \quad (14)$$

Here $\chi = \chi_0$ and $\Omega = \Omega_0$ are model boundary conditions at the anode (i.e. $\xi = 0$; see also Sec. III C), and we highlight that $\Omega = \Omega(\chi)$. Substituting Eqn. 14 into the normalized form of Eqn. 11, rearranging, and then integrating and simplifying gives

$$\bar{I}H_3(\chi) = H_2(\chi) - \alpha \int_0^\xi f^2 d\xi' \quad (15)$$

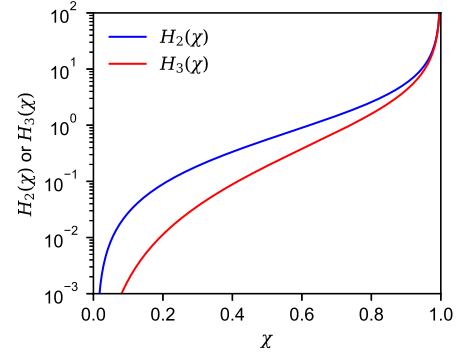


FIG. 3. Special functions $H_2(\chi)$ and $H_3(\chi)$. Here $\chi_0 = 0.01$ and $\Omega_0 = 0.001$ (see also Sec. III C and Tab. I).

where $\bar{I} = MI_d/(eQ_m)$ is the normalized discharge current, f is the normalized magnetic field profile such that $B = B_{max}f$ with B_{max} the maximum magnetic field, and

$$\alpha = \frac{B_{max}^2 A_{ch} L_{ch}}{Q_m} \sqrt{\frac{e^3 k_B T_g}{m_e^2 K_m^2 \varepsilon_c}} \quad (16)$$

$$H_2(\chi) = \int_{\chi_0}^\chi \frac{t^2 dt}{(1-t)^2 \Omega(t)} \quad (17)$$

$$H_3(\chi) = \int_{\chi_0}^\chi \frac{t^3 dt}{(1-t)^2 \Omega(t)} \quad (18)$$

In obtaining Eqn. 15, we have assumed that K_m is constant, which from Fig. 2 (b), is again a reasonable assumption for electron temperatures above about 5-10 eV. Note that the integrals H_2 and H_3 do not depend on any discharge parameters (only the boundary conditions χ_0 and Ω_0), and so can effectively be treated as special functions (plotted in Fig. 3).

With the implicit solution for the normalized ion flux given in Eqn. 15, all other discharge properties can then be determined in terms of this normalized ion flux from the equations above and which include the ion density, ion velocity, neutral density, ionization rate coefficient, ionization rate, electric field, and electron mobility

$$n = \frac{I_d}{A_{ch}} \sqrt{\frac{M}{e^3 \varepsilon_c}} \left[\frac{\chi^2}{\Omega(\chi)} \right] \quad (19)$$

$$v_i = \sqrt{\frac{e \varepsilon_c}{M}} \left[\frac{\Omega(\chi)}{\chi} \right] \quad (20)$$

$$n_g = \frac{Q_m}{M v_g A_{ch}} [1 - \bar{I}\chi] \quad (21)$$

$$K_{iz} = \frac{A_{ch} \sqrt{e k_B T_g \varepsilon_c}}{L_{ch} Q_m} \left[\frac{\alpha f^2 (1 - \chi)^2 \Omega^2(\chi)}{\chi^4 (1 - \bar{I}\chi)^2} \right] \quad (22)$$

$$S_{iz} = \frac{I_d}{e A_{ch} L_{ch}} \left[\frac{\alpha f^2 (1 - \chi)^2 \Omega(\chi)}{\chi^2 (1 - \bar{I}\chi)} \right] \quad (23)$$

$$E = \frac{\varepsilon_c}{L_{ch}} \left[\frac{\alpha f^2 (1 - \chi) \Omega(\chi)}{\chi^2 (1 - \bar{I}\chi)} \right] \quad (24)$$

$$\mu = L_{ch} \sqrt{\frac{e}{M \varepsilon_c}} \left[\frac{1 - \bar{I}\chi}{\alpha f^2} \right] \quad (25)$$

Once the electric field is known, the electrostatic potential can be found from $E = -d\phi/dz$ by making use of Eqns. 4 and 13

$$\phi = \phi_0 + \varepsilon_c \ln \left(\frac{1 - \chi}{1 - \chi_0} \right) \quad (26)$$

with ϕ_0 the potential at the anode. Note that because of the way in which the model has been constructed, explicit reference to the electron temperature is not needed. The electron temperature can however be determined by equating a given ionization rate coefficient with Eqn. 22 (see Sec. V).

III. DISCHARGE STRUCTURE AND PLASMA PROPERTIES

A. Current-voltage relation

Defining the discharge voltage, ϕ_d , as the voltage drop between the anode and cathode, Eqn. 26 gives

$$\chi_L = 1 - (1 - \chi_0) e^{-\bar{\phi}} \quad (27)$$

where $\chi_L = \chi(\xi = 1)$ and $\bar{\phi} = \phi_d/\varepsilon_c$ is the normalized discharge voltage. Note that since $\chi_0 \ll 1$, we have that $\chi_L \approx 1 - \exp(-\bar{\phi})$. Equation 27 allows us to explicitly determine the normalized discharge current as a function of the discharge voltage from Eqn. 15 applied to the thruster exit

$$\bar{I} = \frac{H_2(\chi_L) - \alpha \int_0^1 f^2 d\xi}{H_3(\chi_L)} \quad (28)$$

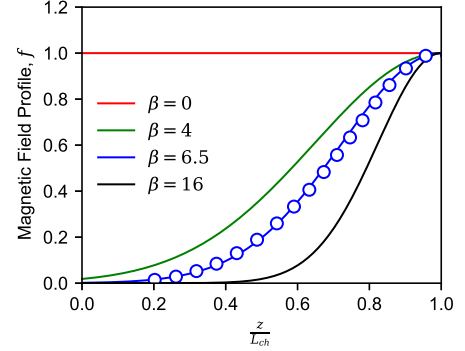


FIG. 4. Magnetic field profile for different values of the control parameter β . The blue markers show the representative profile from Ref. [51].

Note that because of the way in which the discharge current has been defined, it is a positive quantity. Observation of Eqn. 28 then shows that to enforce this constraint we require

$$H_2(\chi_L) \geq \alpha \int_0^1 f^2 d\xi \quad (29)$$

This therefore places a constraint on the minimum discharge voltage for a given value of α (and magnetic field profile, f), or alternatively, a maximum value of α for a given discharge voltage. Since from Eqn. 16 we see that α depends on the propellant mass flow rate and maximum magnetic field strength, Eqn. 29 can also be viewed as placing a constraint on the minimum mass flow rate and maximum magnetic field strength for a given discharge voltage.

B. Magnetic field profile

The model solution in Secs. II B and III A is essentially complete but requires the magnetic field profile as an input. The magnetic field strength in a Hall thruster is usually low near the anode and peaks close to the thruster exit [2, 3]. A convenient mathematical form for the profile commonly used in theoretical and numerical models [27, 33, 46, 47] is a Gaussian given by $f = e^{-\beta(\xi-1)^2}$. Such a profile peaks at the thruster exit and the constant parameter β controls the shape. Figure 4 shows the magnetic field profile for different values of β , as well as a representative profile from Ref. [51].

Using a Gaussian form for the magnetic field in Eqn. 15 allows an explicit solution for position as a function of the normalized ion flux to be obtained

$$\xi = 1 + \frac{1}{\sqrt{2\beta}} \text{erf}^{-1} \left\{ \sqrt{\frac{8\beta}{\pi\alpha^2}} [H_2(\chi) - \bar{I}H_3(\chi)] - \text{erf}(\sqrt{2\beta}) \right\} \quad (30)$$

where erf is the error function and erf^{-1} is the inverse error function. With a Gaussian magnetic field profile, the discharge current-voltage relation (i.e. Eqn. 28) becomes

$$\bar{I} = \frac{H_2(\chi_L) - \sqrt{\frac{\pi\alpha^2}{8\beta}} \text{erf}(\sqrt{2\beta})}{H_3(\chi_L)} \quad (31)$$

or after un-normalizing

$$I_d = \frac{eQ_m}{M} \left[\frac{H_2(\chi_L) - \sqrt{\frac{\pi\alpha^2}{8\beta}} \text{erf}(\sqrt{2\beta})}{H_3(\chi_L)} \right] \quad (32)$$

C. Discharge Structure

To demonstrate the model, we apply it to an example Hall thruster with geometric and operating parameters representative of the SPT-100 [36, 45, 52], and which are listed in Tab. I. At the nominal mass flow rate in Tab. I, Fig. 5 shows the discharge current-voltage characteristic (obtained from Eqn. 32). Here, the minimum voltage needed to initiate a stable discharge is just below 85 V, and the current rapidly increases before saturating for voltages above about 200 V. At higher voltages, the discharge current is almost constant (consistent with experiment; see for example Ref. [53]), and never exceeds the maximum current limit imposed by the input mass flow rate (horizontal black dashed line in Fig. 5). In reality, due to anomalous electron cross-field transport (which is not included in the model), the discharge current for a given discharge voltage can be higher than this limit, although the time-averaged ion current is always lower.

Saturation of the discharge current at high voltages is easily understood from the fact that once all of the propellant is ionized, the current cannot physically increase further (noting of course the possible exception related to enhanced electron transport). This limit can also be seen mathematically from Eqn. 32, since with the aid of Fig. 3, at large voltages $H_2(\chi_L) \gg \sqrt{\pi\alpha^2/(8\beta)} \text{erf}(\sqrt{2\beta})$ and $H_3(\chi_L) \rightarrow H_2(\chi_L)$. Thus, $I_d \rightarrow eQ_m/M$.

Two points marked A and B are indicated on the current-voltage curve in Fig. 5 at voltages of 85 V and 250 V, and which are example cases with low and high neutral depletion. Axial profiles of various plasma properties for these two cases are shown in Figs. 6 and 7 respectively. Figure 6 (a) demonstrates that only a small amount of neutral depletion occurs along the length of the thruster channel for case A, while the plasma density

Parameter	Value
R_1	3.5 cm
R_2	5 cm
L_{ch}	2.5 cm
B_{max}	20 mT
Q_m	5 mg/s
ϕ_d	250 V
β	4
T_g	700 K
K_m	$2.5 \times 10^{-13} \text{ m}^3/\text{s}$
ε_c	25 eV
M	131.293 u (xenon)
χ_0	0.01
Ω_0	0.001

TABLE I. Representative Hall thruster geometric and operating parameters, and model boundary conditions.

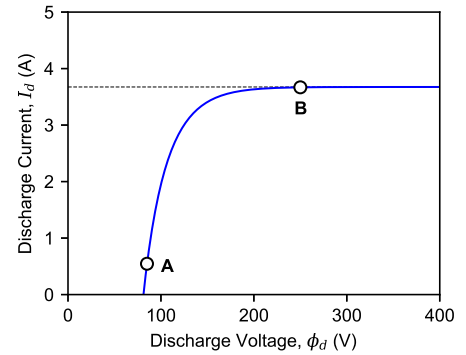


FIG. 5. Discharge current as a function of discharge voltage for the example Hall thruster in Tab. I. The horizontal black dashed line shows the achievable current if all input propellant is ionized. The indicated points A and B denote operation at discharge voltages of 85 V and 250 V respectively.

shows a distinct peak just upstream of the channel center. Ions are accelerated along the channel, as illustrated in Fig. 6 (b), and the final velocity is similar to that measured experimentally at a comparable discharge voltage [54]. We note however that in real Hall thrusters, the discharge extends downstream of the thruster exit plane. Consequently, the total discharge voltage is that between the anode and some location within the near-plume region. In the present model, the plume is not treated and so the discharge voltage is defined as the voltage difference between the anode and the thruster exit plane. Thus, while the maximum ion velocity in Fig. 6 (b) (and also Fig. 7 (b); see below) is similar to that observed experimentally at a similar discharge voltage, the effective length over which this discharge voltage occurs is different. Therefore, the plasma profiles are “distorted” near the exit. Figure 6 (c) shows the ionization rate and the axial electric field, where it is seen that the ionization

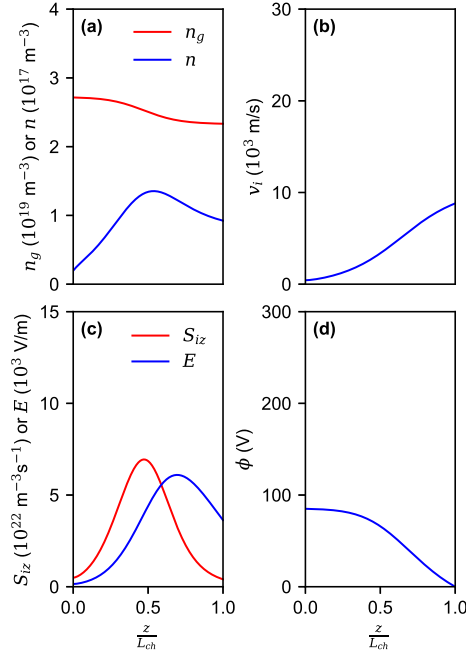


FIG. 6. Axial profiles of the (a) neutral and plasma densities, (b) ion velocity, (c) ionization rate and axial electric field, and (d) electrostatic potential for case A in Fig. 5. The discharge voltage is 85 V and the mass flow rate is 5 mg/s.

rate peaks upstream of the electric field maximum. The electric field peak is broad, which results in an electrostatic potential that varies relatively gradually along the channel (Fig. 6 (d)).

In contrast to Fig. 6, the plasma behaviour in Fig. 7 for case B shows several important differences. Firstly, although the plasma density again peaks inside the channel at a similar location (Fig. 7 (a)), significant neutral depletion now occurs and the neutral gas density near the thruster exit is very low. Ions are also more strongly accelerated within the channel and the ion velocity begins to saturate at the channel exit, with an exit velocity almost twice that of case A (Fig. 7 (b)). The maximum ion velocity is also close to that measured experimentally at the same discharge voltage [54]. As illustrated in Fig. 7 (c), the ionization rate and electric field again peak in a similar location to case A, but the electric field magnitude has increased considerably, and the width of the electric field peak is narrower, leading to a more distinct separation of ionization and acceleration zones. This narrower electric field then naturally leads to a stronger variation of the electrostatic potential, as seen in Fig. 7 (d).

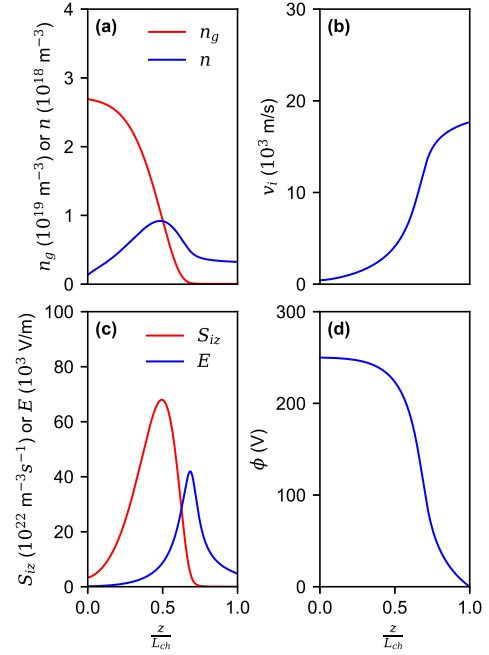


FIG. 7. Axial profiles of the (a) neutral and plasma densities, (b) ion velocity, (c) ionization rate and axial electric field, and (d) electrostatic potential for case B in Fig. 5. The discharge voltage is 250 V and the mass flow rate is 5 mg/s.

In Eqn. 19, an equation for the plasma density was obtained that does not explicitly depend on the magnetic field or axial position. This therefore immediately allows the flux location and magnitude of the maximum plasma density to be determined by setting $\frac{dn}{dx} = 0$, which yields the following implicit equation

$$\chi^2 + 3\chi + 4\ln(1 - \chi) + \frac{\chi}{1 - \chi} = 0 \quad (33)$$

Solving the above equation numerically gives $\chi_{max} = 0.61$. Substituting this into Eqn. 19 yields

$$n_{max} \approx \frac{0.69I_d}{A_{ch}} \sqrt{\frac{M}{e^3\epsilon_c}} \quad (34)$$

Thus, the maximum plasma density is proportional to the discharge current, and inversely proportional to the channel cross-sectional area. The spatial location of the density maximum is obtained from Eqn. 30, and is seen to be a function of the magnetic field profile, discharge current, and parameter α . For the example values in

Tab. I, the normalized location of the density maximum is $\xi_{max} \approx 0.48$ for case B.

Determination of the peak ionization rate and electric field locations can in principle be obtained from Eqns. 23 and 24, but the resulting expressions are quite cumbersome and so must be solved numerically. The peak location of the density, ionization rate, and electric field are shown in Fig. 8. Here it is seen that the plasma density and ionization rate peak at a similar location, diverging only at low discharge voltages. As expected, the electric field always peaks downstream of the ionization rate. For discharge voltages between about 80-150 V, the peak electric field first moves upstream, but at higher discharge voltages, it shifts downstream towards the thruster exit. Because of this, the peak location for cases A and B is similar. The shift in peak electric field is difficult to clearly understand from Eqn. 24 and is effectively a consequence of the need to maintain current balance in the discharge. As the discharge voltage increases, so too does the discharge current. In addition, the plasma density and ion velocity increase while their spatial profiles change, which then influences the neutral gas density and electron mobility. In order to maintain current balance, this initially shifts the peak electric field upstream, but as the discharge voltage is increased above 150 V, neutral depletion becomes important (which strongly affects the electron mobility) and the peak electric field then moves downstream.

Since the plasma density and ionization rate peak at a similar location for high voltages, we can obtain an approximate expression for the maximum ionization rate by setting $\xi_{max} \approx 0.48$ and $\chi_{max} \approx 0.61$ in Eqn. 23, and assuming $\bar{I} \approx 1$. This gives

$$S_{iz,max} \approx \frac{0.065 B_{max}^2 I_d}{Q_m} \sqrt{\frac{ek_B T_g}{m_e^2 K_m^2 \epsilon_c}} \quad (35)$$

We highlight that the location of the maximum ionization rate and electric field depends somewhat on the normalized ion flux and momentum flux at the anode (i.e. χ_0 and Ω_0). This can approximately be seen from Eqns. 23 and 24 and noting that the ionization rate and electric field are inversely proportional to χ^2 . Thus, $S_{iz} \rightarrow \infty$ and $E \rightarrow \infty$ as $\chi_0 \rightarrow 0$. While this divergence at the anode does not affect all plasma properties, or any of the performance metrics (see Sec. IV A), it does imply that χ_0 and Ω_0 must be non-zero (which would also be true if the original model differential equations in Sec. II A were integrated numerically). As long as χ_0 and Ω_0 are small though (which is true in reality), they do not have a significant effect on the thruster behaviour and performance.

The need for non-zero values of χ_0 and Ω_0 is effectively a consequence of neglecting the electron pressure in Eqn. 5. Similar non-zero boundary conditions were required in Ref. [45] where the electron pressure was also ignored. In reality, electron pressure can be important and a plasma

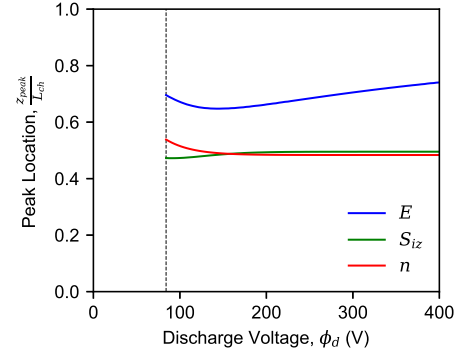


FIG. 8. Normalized axial location of the peak plasma density, ionization rate, and axial electric field as a function of discharge voltage. The vertical black dashed line denotes the minimum voltage needed to sustain a stable plasma discharge. The mass flow rate is 5 mg/s.

sheath may form at the anode leading to ion backflow. As the sheath is very thin, the anode boundary conditions used in several previous models [27, 33, 37, 46] are typically those at the sheath edge where the ion velocity is equal to the Bohm velocity (i.e. the ion flow is sonic) and directed towards the anode. In this case, the ionization zone is detached from the anode and located between the anode and the thruster exit plane (similar to Figs. 6 (c) and 7 (c)). Note also that in this case there are actually two sonic points: one located at the anode with an ion velocity directed towards the anode, and a second point located somewhere between the anode and cathode with an ion velocity directed towards the thruster exit [27, 46]. Ignoring electron pressure in the present model therefore has several implications. Firstly, a plasma sheath cannot form and so ion backflow is not possible. Secondly, the neutral density in the near-anode region is slightly different because backflowing ions can recombine at the anode and increase the local neutral density. These factors are then expected to have a small influence on the plasma discharge. We note as well that some studies, such as that in Ref. [27], have also investigated the effect of a zero ion velocity at the anode. Here, the plasma density and ionization rate now peak at the anode. There is also a less defined separation between the ionization and acceleration regions within the thruster, which is not typically observed experimentally or with higher fidelity models [2, 24, 30, 32].

IV. THRUSTER PERFORMANCE

A. Performance metrics

Ignoring the contribution from neutrals, and remembering that electron pressure has been neglected, the model thrust is given by

$$F = Q_i v_{i,L} = I_d \sqrt{\frac{M \varepsilon_c}{e}} [\Omega(\chi_L)] \quad (36)$$

where $v_{i,L}$ and Q_i are the ion velocity and mass flow rate at the thruster exit. Because of ion beam divergence in real thrusters, as well as the formation of multiply-charged ion species, the actual thrust is expected to be lower than that predicted by Eqn. 36 by as much as 10-20% (see for example Refs. [2, 55]). To approximately account for these factors (which are not included in the model), we introduce a constant thrust correction factor, η_D , such that $F = \eta_D I_d \sqrt{M \varepsilon_c / e} [\Omega(\chi_L)]$. The anode specific impulse is then

$$I_{sp} = \frac{F}{Q_m g_0} = \frac{\eta_D I_d}{Q_m g_0} \sqrt{\frac{M \varepsilon_c}{e}} [\Omega(\chi_L)] \quad (37)$$

with g_0 the gravitational acceleration at sea level. The current efficiency is

$$\eta_c = \frac{\Gamma_L}{\Gamma_d} = \chi_L = 1 - (1 - \chi_0) e^{-\bar{\phi}} \quad (38)$$

while the propellant mass utilization efficiency is

$$\eta_m = \frac{Q_i}{Q_m} = \frac{M I_d}{e Q_m} [\chi_L] \quad (39)$$

The discharge power is

$$P_d = I_d \phi_d \quad (40)$$

while the thrust-to-power ratio is obtained by dividing the thrust by Eqn. 40

$$\frac{F}{P_d} = \frac{\eta_D}{\phi_d} \sqrt{\frac{M \varepsilon_c}{e}} [\Omega(\chi_L)] \quad (41)$$

The electrical efficiency is defined as

$$\eta_e = \left(\frac{v_{i,L}}{v_{i,max}} \right)^2 = \frac{\varepsilon_c}{2 \phi_d} \left[\frac{\Omega^2(\chi_L)}{\chi_L^2} \right] \quad (42)$$

where $v_{i,max} = \sqrt{2e\phi_d/M}$. Finally, the anode thruster efficiency is

$$\eta_T = \frac{F^2}{2Q_m P_d} = \frac{\eta_D^2 M \varepsilon_c I_d}{2e Q_m \phi_d} [\Omega^2(\chi_L)] \quad (43)$$

Using the equations above, the anode thruster efficiency can also be written as: $\eta_T = \eta_D^2 \eta_c \eta_e \eta_m$.

B. Xenon

Again considering the geometric and operating parameters listed in Tab. I, Figs. 9 and 10 show the thrust, anode specific impulse, and various efficiencies as a function of discharge voltage and mass flow rate respectively. The model predictions are compared with existing experimental data for the SPT-100 thruster taken from Ref. [48]. As mentioned in Sec. IV A, the model does not account for ion beam divergence or the formation of multiply-charged ion species. Consequently, to reflect the uncertainty in the predicted thruster performance we use a range of thrust correction factors, η_D (between 0.8-1), which are representative of values measured experimentally [2, 55]. The dashed black lines in Figs. 9 and 10 show the maximum possible performance. This is obtained by ignoring beam divergence and multiply-charged ion species, and assuming that all propellant is ionized and accelerated through the full discharge voltage (i.e. $F = Q_m v_{i,max}$ and $I_{sp} = v_{i,max}/g_0$).

As demonstrated in Fig. 9, and as noted previously in Sec. III A, for a given geometry, magnetic field, and mass flow rate, a minimum discharge voltage is needed to sustain a stable plasma discharge. As the voltage increases, the thrust, specific impulse, and anode thruster efficiency all increase. Similarly, the mass utilization efficiency is a function of voltage (since it is proportional to the discharge current; see Eqn. 39). By contrast, the current and electrical efficiencies do not vary as strongly, which can be seen from Eqns. 38 and 42 where these quantities depend only on the discharge voltage and not the discharge current. In fact, within the context of the present model, these efficiencies also do not depend on the thruster geometric dimensions or magnetic field. Despite the model assumptions, the predicted thrust and specific impulse are generally consistent with experimental values. The thruster efficiency however, is naturally overestimated as plasma-wall energy losses and anomalous electron transport have been neglected. As noted in Sec. III C, the maximum value of the normalized discharge current is 1. However, due to anomalous electron transport, the normalized discharge current can be above 1. Indeed, for the SPT-100 conditions in Fig. 9, the experimental normalized discharge current is around 1.2. Consequently, for the same discharge voltage the discharge power is higher, which then reduces the thruster efficiency by the same factor. The model therefore provides an upper limit of the performance that can be obtained.

Figure 10 shows the thruster performance as a function of mass flow rate for a fixed discharge voltage of 250 V. At this voltage, a minimum mass flow rate just above 0.01 mg/s is needed to sustain a stable discharge. As the mass flow rate increases, the thrust initially rapidly increases before becoming roughly linearly proportional to the mass flow rate (black dashed line in Fig. 10 (a)). The anode specific impulse also rapidly increases before saturating between about 1400-1800 s depending

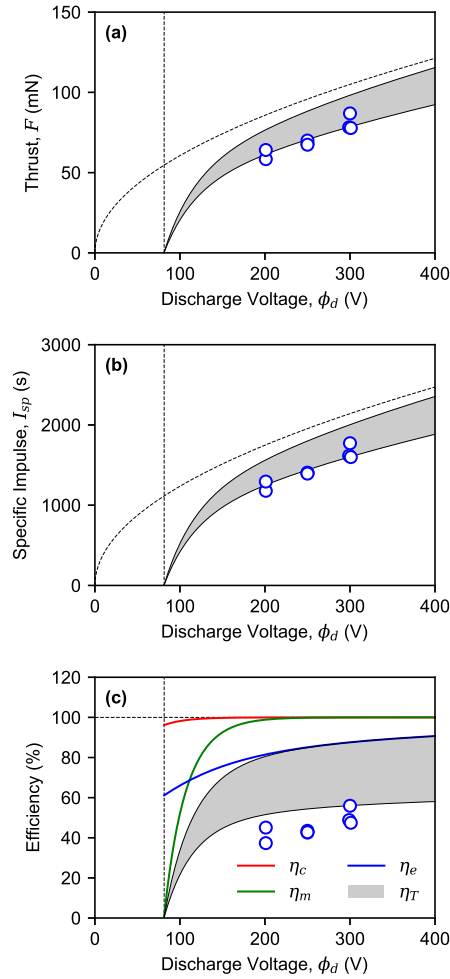


FIG. 9. (a) Thrust, (b) anode specific impulse, and (c) various efficiencies as a function of discharge voltage for a mass flow rate of 5 mg/s. The experimental data points for the SPT-100 thruster have been taken from Ref. [48]. The shaded regions show model predictions for thrust correction factors (i.e. η_D) between 0.8-1. The vertical black dashed lines in (a)-(c) denote the minimum voltage needed to sustain a stable discharge, while the other dashed curves in (a)-(c) show upper limit performance for an ideal thruster.

on the thrust correction factor. Such a saturation is expected since the applied discharge voltage imposes an absolute maximum possible specific impulse (horizontal black dashed line in Fig. 10 (b)). As highlighted previously, since the current and electrical efficiencies depend only on the normalized discharge voltage, they remain constant with mass flow rate, as indicated in Fig. 10 (c). The mass utilization efficiency however varies with mass flow rate as the discharge current is a function of mass flow rate (via the similarity parameter α). Similar to Fig. 9, the predicted thrust and specific impulse are in reasonable agreement with experimental measurements, while the thruster efficiency is overestimated.

C. Similarity parameters

Observation of Eqn. 31 and Eqns. 36-43 show that thruster performance effectively depends only on the normalized discharge voltage, $\bar{\phi} = \phi_d/\varepsilon_c$, and the parameter $\bar{\alpha}$ defined as

$$\bar{\alpha} = \sqrt{\frac{\pi\alpha^2}{8\beta}} \operatorname{erf}(\sqrt{2\beta}) \quad (44)$$

For the model to produce a physical solution, we require not only that the discharge current be greater than zero, but also that the mass utilization efficiency be less than one. From Eqns. 31 and 39, this therefore constrains the values that the parameter $\bar{\alpha}$ can take

$$H_2(\chi_L) - \frac{H_3(\chi_L)}{\chi_L} \leq \bar{\alpha} \leq H_2(\chi_L) \quad (45)$$

Figure 11 shows a plot of $\bar{\alpha}$ as a function of $\bar{\phi}$. Here, the grey shading indicates the parameter region satisfying the above constraints. It can be seen that for a given discharge voltage and energy loss, a feasible discharge is only obtained if $\bar{\alpha}$ is within a certain range. For example, at a normalized discharge voltage of 4, if $\bar{\alpha}$ is above about 25, electron transport across the magnetic field is insufficient and it is difficult, or impossible, to sustain a stable discharge. By contrast, if $\bar{\alpha}$ is below about 2, electron transport and energy gain is now too high. This produces intense ionization and neutral depletion, and leads to an unphysical negative neutral density in some parts of the discharge.

For many high-performance Hall thrusters, the mass utilization efficiency varies between 80-90%, while the anode efficiency varies between about 50-60% [2, 48]. Using Eqns. 31, 39, and 43, we can identify two “laws” governing discharge operation and performance

$$\bar{\alpha} = H_2(\chi_L) - \frac{\eta_m H_3(\chi_L)}{\chi_L} \quad (46)$$

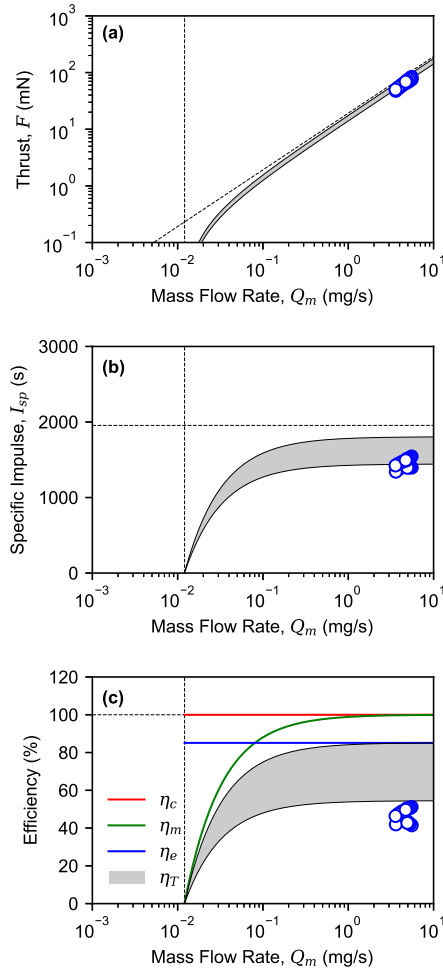


FIG. 10. (a) Thrust, (b) anode specific impulse, and (c) various efficiencies as a function of mass flow rate for a discharge voltage of 250 V. The experimental data points for the SPT-100 thruster have been taken from Ref. [48]. The shaded regions show model predictions for thrust correction factors (i.e. η_D) between 0.8-1. The vertical black dashed lines in (a)-(c) denote the minimum voltage needed to sustain a stable discharge, while the other dashed curves in (a)-(c) show upper limit performance for an ideal thruster.

$$\bar{\alpha} = H_2(\chi_L) - \frac{2\eta_T \bar{\phi} H_3(\chi_L)}{\eta_D^2 \Omega^2(\chi_L)} \quad (47)$$

The blue shading in Fig. 11 (a) shows the sub-area (obtained from Eqn. 46) within the feasible operational region where a mass efficiency of 80-90% is obtained. Similarly, the blue shading in Fig. 11 (b) shows the feasible operational region (obtained from Eqn. 47) where the anode efficiency is between 50-60%. In both cases, such target efficiencies significantly narrow the operating region.

In the form given by Eqn. 16, a clear physical interpretation of the parameter α is not immediately obvious. However, noting that the neutral density without a plasma is $n_{g,0} = Q_m / (M v_g A_{ch})$, a nominal momentum transfer collision frequency can be defined as $\nu_{m,0} = n_{g,0} K_m$. A characteristic ion “transit time frequency” given by $\nu_t = v^* / L_{ch}$ can also be defined. Equation 16 can then be written in the alternative form

$$\alpha = \left(\frac{m_e}{M} \right) \left(\frac{\omega_{max}}{\nu_{m,0}} \right) \left(\frac{\omega_{max}}{\nu_t} \right) \quad (48)$$

where $\omega_{max} = e B_{max} / m_e$. Thus, α is the product of three ratios: the electron to ion mass ratio, the electron cyclotron to the nominal momentum transfer collision frequency, and the electron cyclotron to transit time frequency.

D. Krypton versus xenon

Xenon has typically been the propellant of choice for Hall thrusters because of its attractive properties (such as a relatively high storage density and atomic mass, and a relatively low ionization threshold). However, xenon is expensive and global production limited [56]. In addition, the xenon market is susceptible to strong fluctuations and disruption [57]. Given the rapid growth of the space industry, it is anticipated that demand may outpace supply in the near future [58]. Consequently, alternative propellants have become an important research topic. While iodine has been identified as one possible alternative, several challenges associated with material compatibility and hollow cathode operation remain [59–62]. A short term solution is therefore the use of krypton.

From practical engineering considerations, power input to a propulsion system is usually limited by the satellite power generation capability. Therefore, in shifting to an alternative propellant, a typical engineering constraint that may be imposed is that the maximum thruster power cannot be increased. Similarly, the thruster dimensions and power processing unit ideally may need to remain similar. In this case, both the maximum discharge voltage and discharge current are also limited.

With the model equations and similarity laws obtained, insight can be gained into the operation of Hall

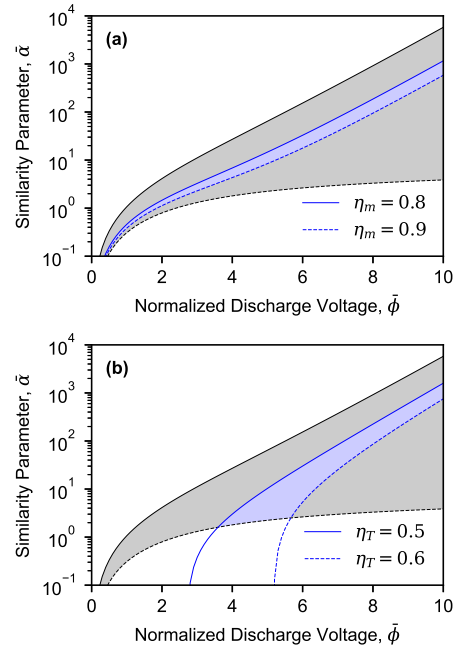


FIG. 11. Similarity parameter map for feasible general operation (grey shaded region), and feasible high-performance operation (blue shaded region) for (a) a mass utilization efficiency between 80-90% and (b) an anode efficiency between 50-60%. Here $\eta_D = 0.9$.

thrusters with alternative propellants. For example, consider a thruster using xenon and which must shift to krypton. To preserve the same anode efficiency for a given discharge voltage, and noting that the collisional energy loss for xenon and krypton is similar (see Fig. 2 (a)), it is seen from Eqn. 43 (remembering that $\tilde{I} = MI_d/(eQ_m)$) that the normalized discharge current must remain the same. If from engineering considerations the maximum discharge current must also be the same, this implies that when using krypton, the propellant mass flow rate must be reduced in proportion to the krypton-xenon atomic mass ratio. From Eqn. 31 however, for the same normalized discharge voltage and current, the similarity parameter $\tilde{\alpha}$ must also remain the same. But from Eqn. 16, the parameter α depends on the mass flow rate. In addition, it also depends on the momentum transfer rate coefficient. Consequently, to preserve the same value of α when shifting to krypton (where now the mass flow rate and momentum transfer rate coefficient are both lower), requires the thruster geometry or magnetic field strength to be changed.

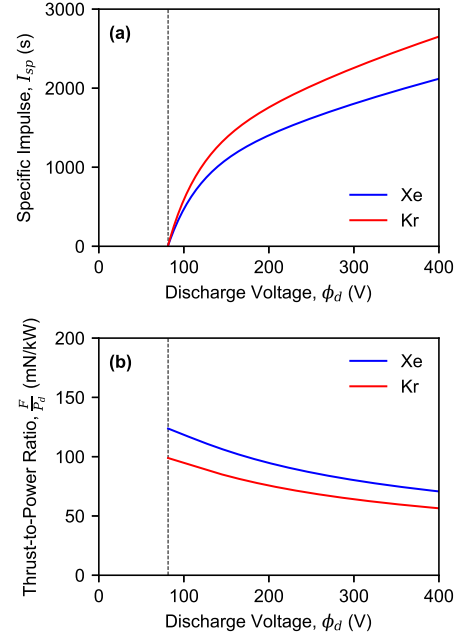


FIG. 12. (a) Specific impulse and (b) thrust-to-power ratio as a function of discharge voltage for thrusters using xenon and krypton propellants. The vertical black dashed lines in (a)-(b) denote the minimum voltage needed to sustain a stable plasma discharge. Here $\varepsilon_c = 25$ eV and $\eta_D = 0.9$, while the mass flow rate and maximum magnetic field when using xenon and krypton are 5 mg/s and 20 mT and 3.2 mg/s and 15 mT respectively.

preserve the same anode efficiency at a target discharge voltage of 250 V, and using a krypton momentum transfer rate coefficient of about 2×10^{-13} m³/s (see Fig. 2 (b)), the mass flow rate decreases from 5 mg/s to about 3.2 mg/s, while the magnetic field strength decreases from 20 mT to around 15 mT. Figure 12 shows a plot of the resulting specific impulse and thrust-to-power ratio, where the specific impulse increases by a factor of 1.25 (equal to the square root of the xenon-krypton mass ratio), while the thrust-to-power ratio decreases by the same amount. This can also be seen from Eqn. 41, since for the same discharge voltage and collisional energy loss, the thrust-to-power ratio is directly proportional to the square root of the propellant atomic mass M .

V. DISCUSSION AND CONCLUSIONS

In this paper, we have presented a one-dimensional theoretical model of a Hall thruster and obtained an analytical solution of the underlying differential equations. The model has been applied to an example thruster and we have studied the plasma discharge properties and system performance. Several key similarity parameters emerge that govern thruster operation and which include the normalized discharge voltage ($\bar{\phi}$), the normalized discharge current (\bar{I}), and an amalgamated parameter that contains all thruster geometric and magnetic field information ($\bar{\alpha}$). In addition, an analytical expression for the discharge current-voltage characteristic that connects all of these similarity parameters together has been obtained, as well as analytical expressions for several important performance metrics.

Within the context of the present model, a stable solution is only obtained if the discharge current is positive and the mass utilization efficiency below one. This therefore imposes constraint relationships between the different similarity parameters. For example, at a given discharge voltage, the similarity parameter $\bar{\alpha}$ must be within a certain range of values. From an operational and design perspective, this indirectly provides constraints and design guidance connecting all of the thruster physical variables: i.e. the main geometric dimensions of the channel, the maximum magnetic field strength, the magnetic field profile, the propellant mass flow rate, the discharge voltage/current, and the propellant type. An example application of the identified similarity parameters to a thruster using the alternative propellant krypton has been presented, where the model provides guidance on thruster optimization. In the particular case where the discharge voltage, current, and anode efficiency are to remain constant when using either xenon or krypton, the model shows that both the mass flow rate and magnetic field strength must simultaneously be reduced.

In order to obtain a tractable mathematical solution, several important assumptions have been made, including: considering a time-independent model, neglecting electron pressure in Eqn. 5, and ignoring electron energy transport and plasma-wall energy losses in Eqn. 7. Time independence means that the presence and excitation of several prevalent and common instabilities, such as the breathing mode [2, 33, 45] and ion transit time instabilities [63], are precluded. While such phenomena can be included (see for example Refs. [24, 30, 45]), the primary aim of the present work was to develop a simplified pedagogical model enabling an analytical solution. Such a solution can provide enhanced understanding and insight, as well as key scaling and similarity parameters. In this sense, a complete analytical model has been obtained. While the functions H_2 and H_3 require a numerical quadrature to compute, they are independent of all thruster geometric and operating parameters and so can effectively be viewed as special functions. We note that aside from enhancing physical understanding, the

analytical model can also find use as one of the few existing theoretical verification solutions for numerical Hall thruster simulations.

Because electron energy transport is not treated, Eqn. 7 represents a local balance between work done on electrons by the electric field and collisional energy losses (which are effectively proportional to the ionization rate; i.e. S_{iz}). Since the continuity equations also depend on the ionization rate, explicit reference to, or indeed calculation of, the electron temperature is not needed. In fact, explicit reference to the ionization rate coefficient (i.e. K_{iz}) is also not required. It can however be determined from the ionization rate since expressions for the plasma and neutral densities are obtained as part of the model solution (see Eqn. 22). By then comparing this ionization rate coefficient with actual rate coefficients obtained by integrating a given electron distribution (such as a Maxwellian) over known ionization cross-sections, the electron temperature can in principle be established. At low discharge voltages where neutral depletion is small, this procedure gives reasonable electron temperatures. However, at higher discharge voltages, neutral depletion becomes significant, and in order to maintain the energy balance in Eqn. 7, the electron temperature can reach unphysically high values near the peak electric field location. In reality, such high electron temperatures cannot occur because of electron energy transport and plasma-wall losses. The ionization rate itself does not experience such unphysical values (see Fig. 7 (c)), because the neutral density is very low in this region.

Neglect of plasma-wall energy losses is also an important assumption. Because the electron temperature in Hall thrusters can be as much as a tenth of the discharge voltage [2, 39], intense secondary electron emission due to electron bombardment of the channel walls occurs. This modifies the plasma sheath in front of the walls and leads to significant power losses. For real Hall thrusters, such as the SPT-100 [2, 48], the effective ion beam energy cost is approximately 144 eV, which is about 5-7 times higher than the average collisional energy loss. Consequently, performance of real thrusters is lower than that predicted by the model. While rigorously including such wall losses makes the model equations intractable, the analytical solution can roughly be extended by phenomenologically including all losses in an effective collisional energy loss, ε_{eff} , and then making the substitution: $\varepsilon_c \rightarrow \varepsilon_{eff}$. As noted in Sec. III A, a minimum discharge voltage is required for the discharge current to be positive. Again using the representative values from Tab. I and $\varepsilon_{eff} = 144$ eV, $\alpha \approx 18$ which gives a minimum discharge voltage of around 330 V. This is much higher than that observed experimentally [64], which is typically around 100 V. As the parameter α is inversely proportional to the momentum transfer rate coefficient, classical electron-neutral collisions alone are not sufficient. Electron cross-field transport must therefore be anomalously high, as is well-known and observed in most, if not all,

Hall thrusters [1, 2]. This represents another important assumption in the model, which is that electron transport is classical.

First principles modelling of anomalous electron transport is difficult and remains a distinct challenge within the community [1]. Current evidence suggests that it is a multi-dimensional kinetic phenomenon [28, 32, 65] that cannot be described with conventional fluid models, regardless of their dimensionality. Nonetheless, phenomenologically viewing anomalous transport as increasing the momentum transfer rate coefficient allows the model to again be extended by making the substitution: $K_m \rightarrow K_{eff}$ where K_{eff} represents an effective rate

coefficient accounting for all possible electron transport mechanisms (e.g. classical and anomalous). Reproducing the minimum discharge voltages observed for the SPT-100 when using $\varepsilon_{eff} = 144$ eV, requires $K_{eff}/K_m \sim 10$.

DATA AVAILABILITY

The datasets generated or used during this study are available on Zenodo: DOI <http://dx.doi.org/10.5281/zenodo.13132001>.

- [1] I. D. Kaganovich, A. Smolyakov, Y. Raitses, E. Ahedo, I. G. Mikelides, B. Jorns, F. Taccogna, R. Gueroult, S. Tsikata, A. Bourdon, *et al.*, Physics of $e \times b$ discharges relevant to plasma propulsion and similar technologies, *Physics of Plasmas* **27** (2020).
- [2] D. M. Goebel, I. Katz, and I. G. Mikelides, *Fundamentals of electric propulsion* (John Wiley & Sons, 2023).
- [3] J.-P. Boeuf, Tutorial: Physics and modeling of hall thrusters, *Journal of Applied Physics* **121** (2017).
- [4] A. Anders and Y. Yang, Direct observation of spoke evolution in magnetron sputtering, *Applied Physics Letters* **111** (2017).
- [5] A. Anders, Tutorial: Reactive high power impulse magnetron sputtering (r-hipims), *Journal of Applied Physics* **121** (2017).
- [6] A. Hecimovic and A. Von Keudell, Spokes in high power impulse magnetron sputtering plasmas, *Journal of Physics D: Applied Physics* **51**, 453001 (2018).
- [7] J. T. Gudmundsson, Physics and technology of magnetron sputtering discharges, *Plasma Sources Science and Technology* **29**, 113001 (2020).
- [8] J. Repp, C. Böhm, J. Crespo López-Urrutia, A. Dörr, S. Eliseev, S. George, M. Goncharov, Y. N. Novikov, C. Roux, S. Sturm, *et al.*, Pentatrap: a novel cryogenic multi-penning-trap experiment for high-precision mass measurements on highly charged ions, *Applied Physics B* **107**, 983 (2012).
- [9] F. Hoh, Instability of penning-type discharges, *The physics of fluids* **6**, 1184 (1963).
- [10] E. Rodríguez, V. Skoutnev, Y. Raitses, A. Powis, I. Kaganovich, and A. Smolyakov, Boundary-induced effect on the spoke-like activity in $e \times b$ plasma, *Physics of Plasmas* **26** (2019).
- [11] K. Thomassen, Turbulent diffusion in a penning-type discharge, *The Physics of Fluids* **9**, 1836 (1966).
- [12] R. Gueroult, J.-M. Rax, and N. J. Fisch, Opportunities for plasma separation techniques in rare earth elements recycling, *Journal of cleaner production* **182**, 1060 (2018).
- [13] M. Krishnan, M. Geva, and J. Hirshfield, Plasma centrifuge, *Physical Review Letters* **46**, 36 (1981).
- [14] W. Bleakney and J. A. Hipple Jr, A new mass spectrometer with improved focusing properties, *Physical Review* **53**, 521 (1938).
- [15] E. Y. Choueiri, Plasma oscillations in hall thrusters, *Physics of Plasmas* **8**, 1411 (2001).
- [16] J. C. McDowell, The low earth orbit satellite population and impacts of the spacex starlink constellation, *The Astrophysical Journal Letters* **892**, L36 (2020).
- [17] T. F. Munro-O'Brien and C. N. Ryan, Performance of a low power hall effect thruster with several gaseous propellants, *Acta Astronautica* **206**, 257 (2023).
- [18] R. Hofer, R. Lobbia, V. Chaplin, A. L. Ortega, I. Mikelides, J. Polk, H. Kamhawi, J. Frieman, W. Huang, P. Peterson, *et al.*, Completing the development of the 12.5 kw hall effect rocket with magnetic shielding (hermes), in *36th International Electric Propulsion Conference*, Vol. 193 (University of Vienna Austria, 2019) pp. 15–20.
- [19] B. Jorns and T. Lafleur, Foundations of plasmas as ion sources, *Plasma Sources Science and Technology* **32**, 014001 (2023).
- [20] P. Chabert, J. Arancibia Monreal, J. Bredin, L. Popelier, and A. Aanesland, Global model of a gridded-ion thruster powered by a radiofrequency inductive coil, *Physics of Plasmas* **19** (2012).
- [21] K. Hara, I. D. Boyd, and V. I. Kolobov, One-dimensional hybrid-direct kinetic simulation of the discharge plasma in a hall thruster, *Physics of Plasmas* **19** (2012).
- [22] J. W. Koo and I. D. Boyd, Modeling of anomalous electron mobility in hall thrusters, *Physics of Plasmas* **13** (2006).
- [23] F. Taccogna and P. Minelli, Three-dimensional particle-in-cell model of hall thruster: The discharge channel, *Physics of Plasmas* **25** (2018).
- [24] I. G. Mikelides and I. Katz, Numerical simulations of hall-effect plasma accelerators on a magnetic-field-aligned mesh, *Physical Review E* **86**, 046703 (2012).
- [25] J. Perales-Díaz, A. Domínguez-Vázquez, P. Fajardo, E. Ahedo, F. Faraji, M. Reza, and T. Andreussi, Hybrid plasma simulations of a magnetically shielded hall thruster, *Journal of Applied Physics* **131** (2022).
- [26] A. Lopez Ortega, I. G. Mikelides, M. J. Sekerak, and B. A. Jorns, Plasma simulations in 2-d (rz) geometry for the assessment of pole erosion in a magnetically shielded hall thruster, *Journal of Applied Physics* **125** (2019).
- [27] A. Cohen-Zur, A. Fruchtman, J. Ashkenazy, and A. Gany, Analysis of the steady-state axial flow in the hall thruster, *Physics of Plasmas* **9**, 4363 (2002).

- [28] J. Adam, A. Héron, and G. Laval, Study of stationary plasma thrusters using two-dimensional fully kinetic simulations, *Physics of Plasmas* **11**, 295 (2004).
- [29] F. Taccogna and L. Garrigues, Latest progress in hall thrusters plasma modelling, *Reviews of Modern Plasma Physics* **3**, 12 (2019).
- [30] G. Hagelaar, J. Bareilles, L. Garrigues, and J.-P. Boeuf, Role of anomalous electron transport in a stationary plasma thruster simulation, *Journal of Applied Physics* **93**, 67 (2003).
- [31] T. Lafleur, S. Baalrud, and P. Chabert, Theory for the anomalous electron transport in hall effect thrusters. i. insights from particle-in-cell simulations, *Physics of Plasmas* **23** (2016).
- [32] T. Lafleur and P. Chabert, The role of instability-enhanced friction on 'anomalous' electron and ion transport in hall-effect thrusters, *Plasma Sources Science and Technology* **27**, 015003 (2017).
- [33] T. Lafleur, P. Chabert, and A. Bourdon, The origin of the breathing mode in hall thrusters and its stabilization, *Journal of Applied Physics* **130** (2021).
- [34] R. Kawashima, K. Hara, and K. Komurasaki, Numerical analysis of azimuthal rotating spokes in a crossed-field discharge plasma, *Plasma Sources Science and Technology* **27**, 035010 (2018).
- [35] M. K. Scharfe, C. A. Thomas, D. B. Scharfe, N. Gascon, M. A. Cappelli, and E. Fernandez, Shear-based model for electron transport in hybrid hall thruster simulations, *IEEE Transactions on Plasma Science* **36**, 2058 (2008).
- [36] N. Gascon, M. Dudeck, and S. Barral, Wall material effects in stationary plasma thrusters. i. parametric studies of an spt-100, *Physics of Plasmas* **10**, 4123 (2003).
- [37] S. Barral, K. Makowski, Z. Peradzyński, N. Gascon, and M. Dudeck, Wall material effects in stationary plasma thrusters. ii. near-wall and in-wall conductivity, *Physics of Plasmas* **10**, 4137 (2003).
- [38] D. Sydorenko, A. Smolyakov, I. Kaganovich, and Y. Raites, Kinetic simulation of secondary electron emission effects in hall thrusters, *Physics of Plasmas* **13** (2006).
- [39] K. Dannenmayer and S. Mazouffre, Elementary scaling relations for hall effect thrusters, *Journal of Propulsion and Power* **27**, 236 (2011).
- [40] E. Lee, Y. Kim, H. Lee, H. Kim, G. Doh, D. Lee, and W. Choe, Scaling approach for sub-kilowatt hall-effect thrusters, *Journal of Propulsion and Power* **35**, 1073 (2019).
- [41] A. A. Shagayda, On scaling of hall effect thrusters, *IEEE Transactions on Plasma Science* **43**, 12 (2014).
- [42] M. M. Turner, A. Derzsi, Z. Donko, D. Eremin, S. J. Kelly, T. Lafleur, and T. Mussenbrock, Simulation benchmarks for low-pressure plasmas: Capacitive discharges, *Physics of Plasmas* **20** (2013).
- [43] T. Charoy, J.-P. Boeuf, A. Bourdon, J. A. Carlsson, P. Chabert, B. Cuenot, D. Eremin, L. Garrigues, K. Hara, I. D. Kaganovich, *et al.*, 2d axial-azimuthal particle-in-cell benchmark for low-temperature partially magnetized plasmas, *Plasma Sources Science and Technology* **28**, 105010 (2019).
- [44] L. L. Alves, M. M. Becker, J. van Dijk, T. Gans, D. B. Go, K. Stapelmann, J. Tennyson, M. M. Turner, and M. J. Kushner, Foundations of plasma standards, *Plasma Sources Science and Technology* **32**, 023001 (2023).
- [45] J. Boeuf and L. Garrigues, Low frequency oscillations in a stationary plasma thruster, *Journal of applied physics* **84**, 3541 (1998).
- [46] E. Ahedo, P. Martínez-Cerezo, and M. Martínez-Sánchez, One-dimensional model of the plasma flow in a hall thruster, *Physics of plasmas* **8**, 3058 (2001).
- [47] S. Barral and E. Ahedo, Low-frequency model of breathing oscillations in hall discharges, *Physical Review E* **79**, 046401 (2009).
- [48] J. M. Sankovic, J. A. Hamley, and T. W. Haag, Performance evaluation of the russian spt-100 thruster at nasa lerc, in *IEPC Conference*, IEPC-93-094 (1994).
- [49] M. A. Lieberman and A. J. Lichtenberg, *Principles of Plasma Discharges and Materials Processing* (John Wiley & Sons, 2005).
- [50] Biagi-v7.1 database, www.lxcat.net, retrieved on may 6, 2024.
- [51] J. Adam, J.-P. Boeuf, N. Dubuit, M. Dudeck, L. Garrigues, D. Gresillon, A. Heron, G. Hagelaar, V. Kulaev, N. Lemoine, *et al.*, Physics, simulation and diagnostics of hall effect thrusters, *Plasma Physics and Controlled Fusion* **50**, 124041 (2008).
- [52] N. MacDonald-Tenenbaum, Q. Pratt, M. Nakles, N. Pilgram, M. Holmes, and W. Hargus Jr, Background pressure effects on ion velocity distributions in an spt-100 hall thruster, *Journal of Propulsion and Power* **35**, 403 (2019).
- [53] M. R. Nakles, W. A. Hargus Jr, J. J. Delgado, R. L. Corey, and A. F. R. L. E. A. CA, A performance comparison of xenon and krypton propellant on an spt-100 hall thruster (preprint), (2011).
- [54] W. Hargus, Jr and M. Cappelli, Laser-induced fluorescence measurements of velocity within a hall discharge, *Applied Physics B* **72**, 961 (2001).
- [55] J. A. Linnell and A. D. Gallimore, Efficiency analysis of a hall thruster operating with krypton and xenon, *Journal of Propulsion and Power* **22**, 1402 (2006).
- [56] D. A. Herman and K. G. Unfried, Xenon acquisition strategies for high-power electric propulsion nasa missions, in *JANNAF SPS Subcommittee Meeting*, GRC-E-DAA-TN23198 (2015).
- [57] "russia's invasion of ukraine impacts gas markets critical to chip production", <https://www.csis.org/blogs/perspectives-innovation/russias-invasion-ukraine-impacts-gas-markets-critical-chip-production>, retrieved on may 7, 2024.
- [58] D. Rafalskyi, J. M. Martínez, L. Habl, E. Zorzoli Rossi, P. Proynov, A. Boré, T. Baret, A. Poyet, T. Lafleur, S. Dudin, *et al.*, In-orbit demonstration of an iodine electric propulsion system, *Nature* **599**, 411 (2021).
- [59] J. Martínez Martínez and D. Rafalskyi, Design and development of iodine flow control systems for miniaturized propulsion systems, *CEAS Space Journal* **14**, 91 (2022).
- [60] C. Guidi, G. Becatti, L. Bernazzani, A. Ceccarini, F. Paganucci, and M. M. Saravia, Study on the compatibility between iodine and common aerospace materials, *Acta Astronautica* (2024).
- [61] D. Zschätzsch, S. L. Benz, K. Holste, M. Vaupel, F. G. Hey, C. Kern, J. Janek, and P. J. Klar, Corrosion of metal parts on satellites by iodine exposure in space, *Journal of Electric Propulsion* **1**, 14 (2022).
- [62] G. F. Benavides, H. Kamhawi, J. Mackey, T. Haag, and G. Costa, Iodine hall-effect electric propulsion system research, development, and system durability demonstration, in *2018 Joint Propulsion Conference* (2018) p. 4422.

This is the author's peer reviewed, accepted manuscript. However, the online version of record will be different from this version once it has been copyedited and typeset.

PLEASE CITE THIS ARTICLE AS DOI: 10.1063/5.0220130

- [63] V. Kim, Transit-time instability in hall thrusters, *Physics of Plasmas* **12**, 073504 (2005).
- [64] V. Kim, Main physical features and processes determining the performance of stationary plasma thrusters, *Journal of Propulsion and Power* **14**, 736 (1998).
- [65] I. G. Mikellides and A. L. Ortega, Challenges in the development and verification of first-principles models in hall-effect thruster simulations that are based on anomalous resistivity and generalized ohm's law, *Plasma Sources Science and Technology* **28**, 014003 (2019).